J. Fluid Mech. (2011), *vol.* 672, *pp.* 196–218. © Cambridge University Press 2011
doi:10.1017/S0022112010005914

Peristaltic pumping of viscous fluid in an elastic tube

D. TAKAGI[1] AND N. J. BALMFORTH[2,3]†

[1]Institute of Theoretical Geophysics, Department of Applied Mathematics and Theoretical Physics, University of Cambridge, Wilberforce Road, Cambridge CB3 0WA, UK

[2]Department of Mathematics, University of British Columbia, 1984 Mathematics Road, Vancouver, V6T 1Z2, Canada

[3]Department of Earth and Ocean Science, University of British Columbia, 6339 Stores Road, Vancouver, V6T 1Z4, Canada

(Received 14 April 2010; revised 3 November 2010; accepted 10 November 2010; first published online 24 February 2011)

A model is derived for long peristaltic waves propagating steadily down a fluid-filled, axisymmetric tube. The waves are driven by imposing a radial force of prescribed form on the tube. The resulting deformation of the tube wall is modelled using linear elasticity and the internal flow using the lubrication approximation. Numerical solutions for periodic wave trains and solitary waves are presented, along with asymptotic solutions at both small and large forcing amplitudes. Large-amplitude periodic waves are characterized by narrow blisters adjoining long occluded sections of the tube, whereas a solitary wave of strong contraction produces a long inflated bow wave that propels a large quantity of fluid. A measure of pumping efficacy is given by the ratio of the net fluid displacement to the power input, and is highest for a large-amplitude solitary wave.

Key words: lubrication theory, peristaltic pumping, solitary waves

1. Introduction

Many biological ducts, including the digestive system (Brasseur 1987) and the ureter (Yin & Fung 1971), convey their fluid contents by peristalsis – the propulsion of internal fluid by propagating waves of muscular contraction in the surrounding tube wall. Peristaltic pumps operate on the same principle, except that protuberances are usually driven into the tube wall to create waves of fixed wall displacement. The dynamics of fluid flow near undulating boundaries is also fundamental to numerous styles of biological locomotion, including the swimming of micro-organisms (Taylor 1951; Katz 1974; Argentina, Skotheim & Mahadevan 2007; Balmforth, Coombs & Pachman 2010) and the crawling of worms (Keller & Falkovitz 1983) and snails (Chan, Balmforth & Hosoi 2005).

The first models of peristalsis focused on predicting internal fluid motions driven by a given displacement of the confining tube wall (as in the peristaltic pump). To further simplify the fluid mechanics, the models assumed either low-amplitude waves or adopted lubrication theory, which is relevant when the fluid flow has low Reynolds number and the peristaltic waves are relatively long (Fung & Yih 1968; Shapiro, Jaffrin & Weinberg 1969; Lykoudis & Roos 1970). These theories were later

† Email address for correspondence: njb@math.ubc.ca

extended to non-slender geometries and higher Reynolds numbers (e.g. Pozrikidis 1987; Takabatake, Ayukawa & Mori 1988), with the latest developments directed at, for example, systematic exploration of the effect of the wave profile (Walker & Shelley 2010).

Nevertheless, models of biological ducts demand an inclusion of the solid mechanics of the tube wall, and specifically the muscle action forcing deformation and any material stiffness. A key difficulty with the addition of the tube mechanics is that the shape of the deformable boundary must be determined as part of the solution, rendering the exercise a free-boundary problem. The existing literature treating this version of the problem is much more sparse, and focused largely on the dynamics of the ureter (Fung 1971; Griffiths 1987, 1989; Carew & Pedley 1997) or tailored to other specific biological applications (Miftakhov & Wingate 1994; Szeri *et al.* 2008). In the current article, we approach this problem from a more general perspective, and construct a relatively simple mathematical model that incorporates the solid mechanics of the tube wall. We are thereby able to make analytical inroads into the problem, offering a fairly complete description of the dependence on physical parameters and formulating a number of asymptotic solutions in various limits, as outlined presently. The article by Tang & Rankin (1993) is most closely related to our current effort; they provide some lubrication solutions for a tube modelled as a stretched membrane in which the tension is spatially varied in order to drive peristaltic motion, along with complementary numerical solutions of the corresponding Stokes flow problem. Our model also provides a foundation for a companion paper (Takagi & Balmforth 2011) which explores a particular generalization of the theory in which we include a rigid slender object suspended in the fluid.

In § 2, our model is formulated by stating the underlying assumptions and deriving the governing equations. In § 3, solutions are obtained either analytically for small-amplitude waves or numerically for moderate-amplitude waves. Asymptotic solutions in the limit of large forcing amplitude are presented in § 4, and we conclude in § 5. Appendices A and B construct more asymptotic solutions in the limits of small and large bending stiffness, respectively, and Appendix C describes some additional details of the structure of the large-amplitude solutions.

2. Mathematical formulation

2.1. *Dimensional equations*

Consider steady peristaltic waves running down an axisymmetric tube of radius, $\hat{a}(\hat{z}, t)$, described by a cylindrical polar coordinate system, $(\hat{r}, \hat{z})$, at time t, and filled with an incompressible, viscous fluid of density, ρ, dynamic viscosity, μ, and pressure, $\hat{p}(\hat{r}, \hat{z}, t)$ (as sketched in figure 1). A radial force per unit area, $F(\hat{z} - ct) = \hat{\eta} f[(\hat{z} - ct)/L]$, is applied on the tube wall, where f is a dimensionless function that characterizes the spatial structure of the forcing, the overall amplitude is $\hat{\eta}$, the propagation speed is c, and L is the characteristic axial length scale. Without the forcing, the tube has constant radius, R, and the internal pressure is p_0.

Invoking the lubrication approximation for the velocity field, $(\hat{u}, \hat{w})$, of the induced fluid flow (applying when $R \ll L$, and the Reynolds number, $\rho c R/\mu$, is order one or smaller), conservation of mass and momentum demand that

$$\frac{1}{\hat{r}}\frac{\partial}{\partial \hat{r}}(\hat{r}\hat{u}) + \frac{\partial \hat{w}}{\partial \hat{z}} = 0, \quad \frac{\partial \hat{p}}{\partial \hat{r}} = 0, \quad \frac{\partial \hat{p}}{\partial \hat{z}} = \frac{1}{\hat{r}}\frac{\partial}{\partial \hat{r}}\left(\hat{r}\mu\frac{\partial \hat{w}}{\partial \hat{r}}\right). \tag{2.1}$$

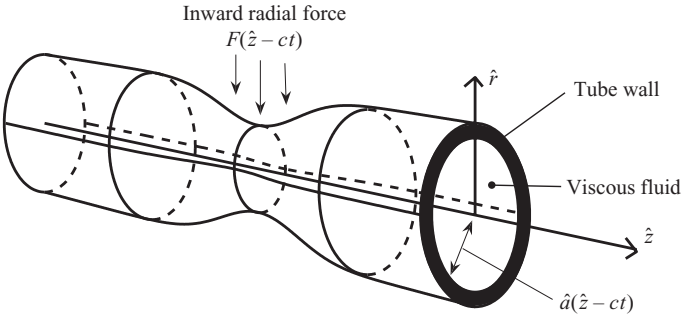

FIGURE 1. A sketch of the geometry, showing the axisymmetric tube and the cylindrical polar coordinate system used to describe it.

For boundary conditions, we impose regularity along the centreline of the tube, $\hat{r}=0$, and allow no slip between the fluid and the tube wall. Since the tube is slender, the fluid resistance is chiefly provided by the normal pressure force; the fluid traction remains much smaller. Consequently, the tube deforms almost radially and

$$\frac{\partial \hat{a}}{\partial t} \equiv -c\frac{\partial \hat{a}}{\partial \hat{z}} = u \quad \text{and} \quad \hat{w}=0 \quad \text{for} \quad \hat{r}=\hat{a} \tag{2.2}$$

(e.g. Skotheim & Mahadevan 2005). For the axial boundary conditions, we consider either periodic domains or an infinitely long tube with any flow disturbances decaying as $\hat{z}\to\pm\infty$ (see Li & Brasseur 1993, for a discussion of end effects with different boundary conditions on a finitely long tube).

For simplicity, we model the cylindrical tube as a linearly elastic material. However, even with this assumption, there is still considerable freedom in choosing a particular model, as the tube could be reinforced in some fashion on the outside or possess a layered structure. If the tube has no reinforcing and is isotropic and sufficiently thin, the classical theory of shells suggests that the force resisting deformation, F_E, is given by

$$F_E = \frac{h^3 E}{12(1-\nu^2)}\frac{\partial^4}{\partial \hat{z}^4}(\hat{a}-R) + \frac{Eh}{R^2}(\hat{a}-R), \tag{2.3}$$

where h is the shell thickness, E is Young's modulus and ν is the Poisson ratio (Timoshenko & Woinowsky-Krieger 1959). Alternatively, if the tube is reinforced and behaves more like an elastic foundation, then the resistance might be modelled by

$$F_E = \frac{E(\hat{a}-R)}{h(1-\nu^2)} - \frac{Eh}{3(1-\nu^2)}\frac{\partial^2}{\partial \hat{z}^2}(\hat{a}-R) \tag{2.4}$$

(the 'Pasternak' foundation, e.g. Kerr 1984). Both (2.3) and (2.4) have the form

$$F_E = \hat{D}\left[(1-\alpha)+\alpha(-1)^{n/2}L^n\frac{\partial^n}{\partial \hat{z}^n}\right](\hat{a}-R), \tag{2.5}$$

where $\hat{D}$ is a stiffness parameter proportional to Young's modulus, $n=2$ or 4, and α is a geometrical factor built from ratios of the length scales R, L and h. In many physical situations, the geometrical factor α is small, leaving $\hat{D}(a-R)$ as the dominant resistive force, which is also the form expected for a slender cylindrical hole in an infinite linear elastic solid. Though potentially less physical, the model (2.5) with $\alpha=1$ allows us to study how a higher-order resisting force like axial bending stiffness ($n=4$) may change the dynamics. Thus, for practical examples, we choose $n=\alpha=0$

or $(n, \alpha) = (4, 1)$, referring to these as the $n = 0$ or $n = 4$ cases, respectively. Thence, $F_E \to \hat{D}L^n \partial^n(\hat{a} - R)/\partial \hat{z}^n$. By considering both cases, we gain a better impression of the effect of solid mechanics. However, we have also verified that the results presented below are qualitatively insensitive to the choice of α and other values of n (indeed, without much further effort, many of the analytical results presented below can be generalized to the full form of (2.5)), with the one major exception described in § 5. The force balance on the elastic tube can now be written as

$$\hat{p}(\hat{a}, \hat{z}, t) - p_0 = \hat{D}L^n \frac{\partial^n}{\partial \hat{z}^n}(\hat{a} - R) + F. \tag{2.6}$$

Note that some of the solutions we present later possess significant elastic displacements, calling into question the validity of linear elasticity; to retain a degree of model simplicity, however, we do not include any effect of nonlinear elasticity.

2.2. *Dimensionless formulation*

We remove the dimensions by transforming to the frame of reference moving with the wave of forcing and defining new coordinates,

$$z = \frac{\hat{z} - ct}{L}, \quad r = \frac{\hat{r}}{R}, \tag{2.7}$$

the scaled variables,

$$[u(r, z), w(r, z)] = \frac{1}{c}(\hat{u}, \hat{w} - c), \quad a(z) = \frac{\hat{a}}{R}, \quad p(r, z) = \frac{(\hat{p} - p_0)R^2}{\mu c L}, \tag{2.8}$$

and dimensionless parameters,

$$D = \frac{\hat{D}R^3}{\mu c L}, \quad \eta = \frac{\hat{\eta}R}{\mu c}, \tag{2.9}$$

representing measures of tube stiffness and forcing strength, respectively, compared to viscous drag in the fluid. We next integrate the dimensionless versions of (2.1) with respect to r and impose the boundary conditions in (2.2) to arrive at the axial velocity in the wave frame,

$$w = \frac{1}{4}\frac{\mathrm{d}p}{\mathrm{d}z}(r^2 - a^2) - 1, \tag{2.10}$$

where the fluid pressure is independent of r and satisfies

$$p = D\frac{\mathrm{d}^n}{\mathrm{d}z^n}(a - 1) + \eta f(z). \tag{2.11}$$

Finally, the integral form of mass conservation is

$$\frac{\mathrm{d}}{\mathrm{d}z}\int_0^a wr \, \mathrm{d}r = 0, \tag{2.12}$$

implying

$$q = 1 - a^2 - \frac{1}{8}\frac{\mathrm{d}p}{\mathrm{d}z}a^4, \tag{2.13}$$

where the constant, q, is proportional to the time-averaged volumetric flow rate in the laboratory frame, $\pi(1 + 2\int_0^a wr \, \mathrm{d}r)$.

2.3. *Periodic waves*

In axially periodic settings, $0 \leqslant z \leqslant 2\pi$, we substitute (2.11) into (2.13), to find

$$q = 1 - a^2 - \frac{1}{8}a^4 \left[D\frac{\mathrm{d}^{1+n}a}{\mathrm{d}z^{1+n}} + \eta f'(z) \right]. \tag{2.14}$$

The constant, q, is determined as an eigenvalue of (2.14) on imposing the constraint,

$$1 = \langle a^2 \rangle \equiv \frac{1}{2\pi}\int_0^{2\pi} a^2 \,\mathrm{d}z, \tag{2.15}$$

which reflects mass conservation and our choice of the undisturbed tube radius as the radial length scale. The constraint further implies

$$q = -\frac{1}{8}\left\langle a^4 \frac{\mathrm{d}p}{\mathrm{d}z} \right\rangle = -\frac{1}{8}\left\langle a^4 \left(D\frac{\mathrm{d}^{1+n}a}{\mathrm{d}z^{1+n}} + \eta f' \right) \right\rangle. \tag{2.16}$$

By way of illustration of periodic waves, we impose a sinusoidal force with

$$f(z) = \sin z. \tag{2.17}$$

2.4. *Solitary waves*

We also consider solitary waves propagating down an infinite duct induced by a spatially localized forcing (i.e. $f \to 0$ for $|z| \gg 1$). In this case, the far-field boundary conditions become $a \to 1$ as $z \to \pm\infty$, which further imply that $q = 0$. The solitary-wave problem is therefore

$$0 = 1 - a^2 - \frac{1}{8}a^4 \left[D\frac{\mathrm{d}^{1+n}a}{\mathrm{d}z^{1+n}} + \eta f'(z) \right]. \tag{2.18}$$

In practice, we solve (2.18) on a finite domain that is sufficiently long for the solution to converge to the far-field level $a = 1$ well before the boundaries of the computational domain.

To replace q as a measure of peristalsis, we define

$$\Delta \equiv \int_{-\infty}^{\infty} \mathrm{d}z \int_0^a 2(w+1)r \,\mathrm{d}r = -\frac{1}{8}\int_{-\infty}^{\infty} a^4 \frac{\mathrm{d}p}{\mathrm{d}z}\,\mathrm{d}z, \tag{2.19}$$

which provides an estimate of the net transport due to the passage of the solitary wave in the laboratory frame. Equivalently (cf. (2.13)),

$$\Delta = \int_{-\infty}^{\infty} (a^2 - 1)\,\mathrm{d}z = -\frac{1}{8}\int_{-\infty}^{\infty} a^4 \left(D\frac{\mathrm{d}^{1+n}a}{\mathrm{d}z^{1+n}} + \eta f' \right) \mathrm{d}z. \tag{2.20}$$

For purposes of illustration, we choose a Gaussian profile for the solitary-wave forcing:

$$f(z) = \exp\left(-\tfrac{1}{2}z^2\right). \tag{2.21}$$

2.5. *Pumping efficacy*

Taking the dot product of the dimensionless versions of the momentum equations in (2.1) with the velocity in the lab frame, $(u, w+1)$, leads to the energy relation,

$$\frac{1}{r}\frac{\partial}{\partial r}\left\{ r\left[up - (w+1)\frac{\partial w}{\partial r} \right] \right\} + \frac{\partial}{\partial z}[(w+1)p] = -\left(\frac{\partial w}{\partial r} \right)^2, \tag{2.22}$$

where the left-hand side represents the divergence of the energy flux and the right-hand side is the local dissipation rate, to leading order in the aspect ratio R/L. Therefore, in the lubrication limit, the total dimensionless rate of energy dissipation in the fluid is

$$\varepsilon = 2\pi \int_{\mathscr{D}} \int_0^a \left(\frac{\partial w}{\partial r}\right)^2 r \, \mathrm{d}r \, \mathrm{d}z, \tag{2.23}$$

where the symbol $\mathscr{D}$ represents the relevant integration limits for either the periodic or infinite axial domain. For our steady peristaltic waves, there is no net pressure drop along the tube, and the dissipation rate is balanced by the power input by the pressure force on the tube wall:

$$\varepsilon = -2\pi \int_{\mathscr{D}} ap[u(r,z)]_{r=a} \, \mathrm{d}z \equiv 8\pi \int_{\mathscr{D}} \frac{(1-q-a^2)^2}{a^4} \, \mathrm{d}z. \tag{2.24}$$

This also means that the mechanical efficiency defined by Shapiro *et al.* (1969), proportional to the rate at which useful energy is stored in the fluid, is identically zero, and so we require an alternative means to estimate the efficacy of the peristaltic waves. Instead, we define pumping efficacy by $2\pi^2 q/\varepsilon$ or $\pi\Delta/\varepsilon$, for periodic and solitary waves, respectively which measure the fluid transport per unit input power.

3. Small to moderate forcing amplitudes

3.1. *The small-amplitude limit*

For small amplitude forcing, $\eta \ll 1$, the equations can be solved using a regular perturbation expansion: $a = 1 + \eta a_1 + \eta^2 a_2 + \cdots$ and $q = \eta^2 q_2 + \cdots$. for periodic waves, or $\Delta = \eta^2 \Delta_2 + \cdots$ for solitary waves. The leading-order perturbation in tube radius satisfies the linear ODE,

$$D\frac{\mathrm{d}^{1+n} a_1}{\mathrm{d}z^{1+n}} + 16 a_1 = -f'(z). \tag{3.1}$$

The degree of transport is given by

$$q_2 = -\frac{1}{2}\langle a_1 f' \rangle \qquad \text{or} \qquad \Delta_2 = \int_{-\infty}^{\infty} a_1^2 \, \mathrm{d}z = -\frac{1}{2}\int_{-\infty}^{\infty} a_1 f' \, \mathrm{d}z. \tag{3.2}$$

With sinusoidal forcing, $f = \sin z$, because the homogeneous solutions to (3.1) are non-periodic and $n = 0$ or 4, the low-amplitude periodic waves are given by

$$a \sim 1 - \eta \frac{(16\cos z + D \sin z)}{(16^2 + D^2)}, \tag{3.3}$$

and

$$q \sim \frac{4\eta^2}{16^2 + D^2}. \tag{3.4}$$

It follows that the dissipation rate is

$$\varepsilon \sim \frac{32\pi^2 \eta^2}{16^2 + D^2}, \tag{3.5}$$

leading to a pumping efficacy of $2\pi^2 q/\varepsilon \sim 1/4$. Note that the solution in (3.3) corresponds to the low-amplitude limit of the earlier models developed by prescribing wall displacements of sinusoidal form (Fung & Yih 1968; Shapiro *et al.* 1969).

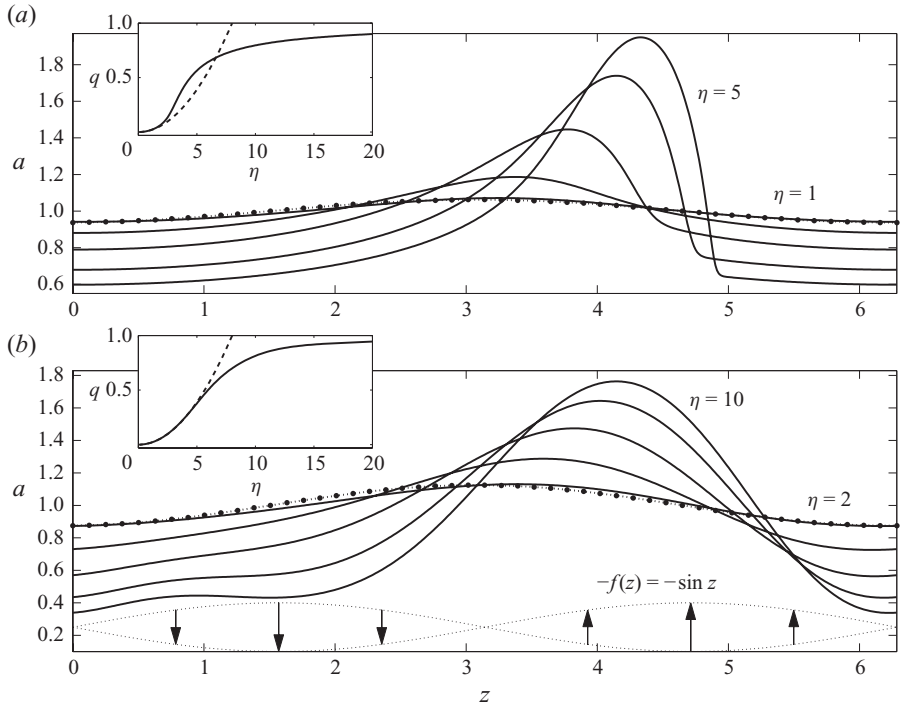

FIGURE 2. Periodic wave profiles with increasing forcing amplitude for (*a*) $n=0$ and $\eta=1, 2, \ldots, 5$, and (*b*) $n=4$ and $\eta=2, 4, \ldots, 10$, with $D=1$. The insets show the flux q against η, with the dashed curves showing the low-amplitude prediction in (3.4). In the main figures, the dots show the low-amplitude solutions (3.3) with either $\eta=1$ or $\eta=2$. The arrows in (*b*) show the magnitude and direction of the applied radial force (as given by $-f(z)=-\sin z$).

Nevertheless, for most of the other solutions that we present, the deformation of the tube wall is a complicated nonlinear function of the forcing.

For the solitary waves with Gaussian forcing, the solution to (3.1) can be reduced to a quadrature that is most compactly written in terms of the inverse Fourier transform,

$$a_1 = \frac{\mathrm{i}}{2\pi}\int_{-\infty}^{\infty} \frac{k\mathrm{e}^{\mathrm{i}kz}\,\bar{f}(k)\,\mathrm{d}k}{(\mathrm{i}k)^{1+n}D-16}, \tag{3.6}$$

where $\bar{f}(k)\equiv\int_{-\infty}^{\infty} f(z)\mathrm{e}^{-\mathrm{i}kz}\,\mathrm{d}z$ denotes the Fourier transform of $f(z)$. The transport coefficient Δ_2 can then be computed numerically from (3.2), and further quadratures furnish the proportionality constant in the limiting dissipation rate, $\varepsilon\propto\eta^2$.

3.2. *Numerical solutions with moderate forcing*

The equations for a, (2.14) and (2.18), can be solved numerically using a relaxation scheme (in practice, we use MATLAB'S BVP4C verifying that the error tolerance assumed has no effect on the solutions computed). A representative set of periodic wave solutions for different forcing amplitudes η is plotted in figures 2(*a*) and 2(*b*) for the two types of elastic tubes, $n=0$ and $n=4$, respectively. The insets in the figure display how the eigenvalue q varies as η sweeps through the values used in the main figures and beyond. As η increases, the tube becomes increasingly deformed and the amount of transport increases. The periodic deformations remain qualitatively similar for both $n=0$ and $n=4$; the tube develops a substantial bulge near $z=3\pi/2$,

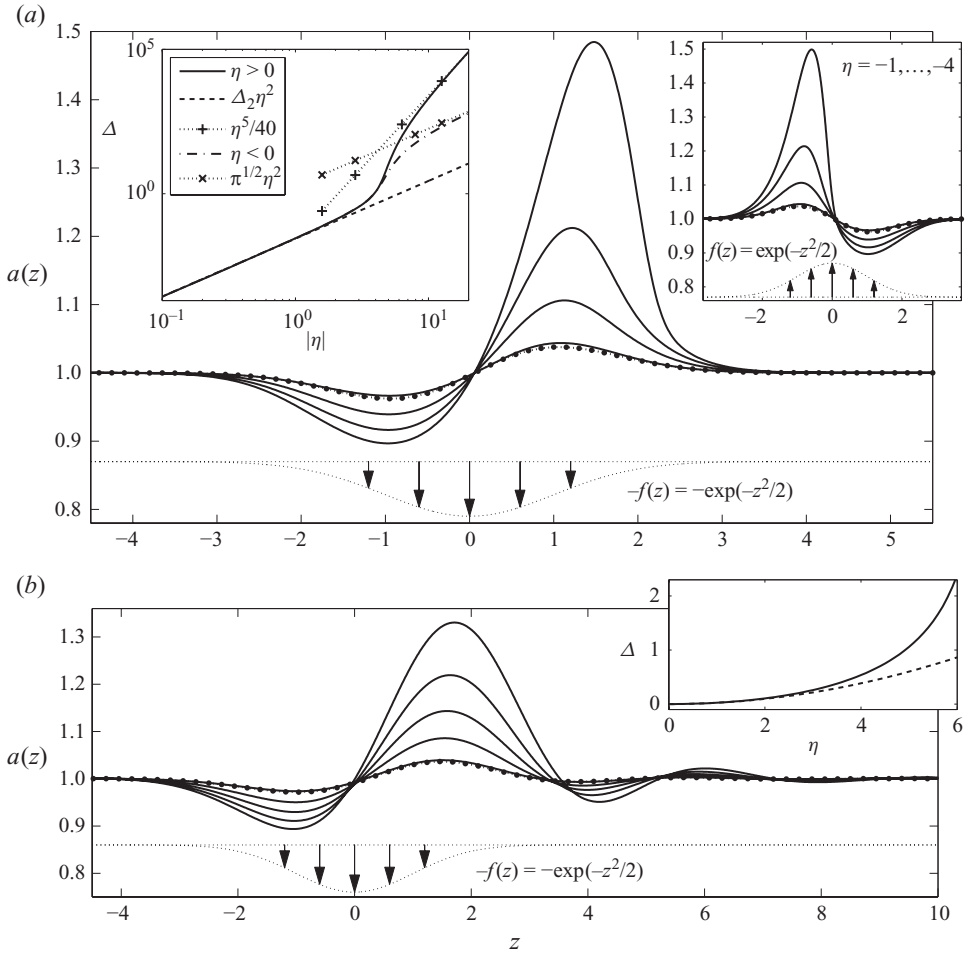

FIGURE 3. Solitary wave profiles for (*a*) $n=0$ and $\eta=1,2,\ldots,4$, and (*b*) $n=4$ and $\eta=1,2,\ldots,5$, with $D=1$. The insets show the transport Δ against η, with the dashed curves showing the low-amplitude prediction, $\Delta_2\eta^2$, computed using (3.2). In (*a*), the plot of the transport also includes the large-amplitude predictions ($\eta^2/40$ and $\pi^{1/2}\eta^2$; § 4), and the second inset shows wave profiles for $\eta=-1$, -2, -3 and -4. The arrows show the magnitude and direction of the applied force (as given by $f(z)$ and the sign of η).

where the *outward* imposed force is highest, and becomes constricted over the longer sections elsewhere.

Figure 3 shows analogous results for solitary-wave profiles. Once more, the results for $n=0$ and $n=4$ are similar, at least for the forcing amplitudes shown. With $f=\exp(-z^2/2)$, there are two possible forcing protocols depending on whether η is taken positive or negative; $\eta>0$ corresponds to a squeezing action, whereas $\eta<0$ describes how a forced expansion conveys fluid. For a low forcing amplitude, the two protocols generate identical amounts of transport (since $\Delta\propto\eta^2$ for $\eta\ll1$); both cases are shown in figure 3(*a*) for $n=0$. At higher forcing amplitudes, the two protocols generate different results, with the forced expansion transporting less fluid than the wave of contraction.

Dissipation rates are plotted against forcing amplitude in figure 4 for $n=0$ and both periodic and solitary waves. For periodic waves, the maximum dissipation is

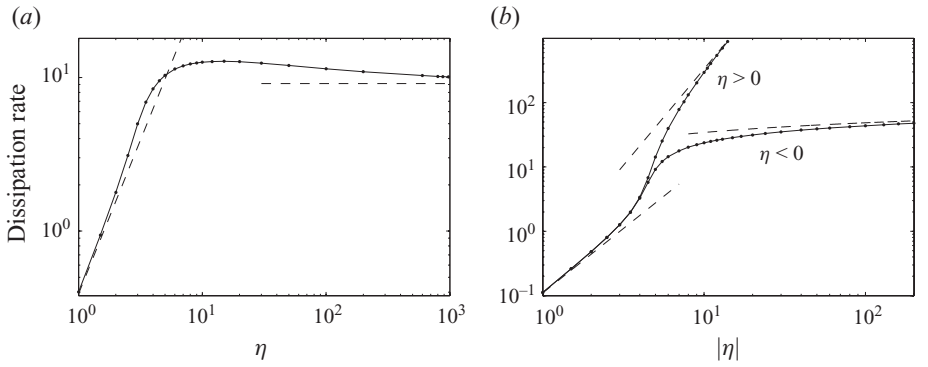

FIGURE 4. Dimensionless dissipation rates versus η with $n=0$ and $D=1$ for (a) periodic and (b) solitary waves. The small- and large-amplitude limits are indicated (given by (3.5) for $\eta \ll 1$ and $\varepsilon \sim 4\pi(2\pi - 4)$ for $\eta \gg 1$ in (a), and $\varepsilon \sim 0.11\eta^2$ for $\eta \ll 1$, and $\varepsilon \sim \eta^3/3D^2$ or $\varepsilon \sim 16\sqrt{2\log(-\eta/D)}$ for $|\eta| \gg 1$ in (b); see §§ 3.1 and 4).

attained at a moderate forcing amplitude and ε decays towards a constant in the large-amplitude limit. For solitary waves, the dissipation rate continues to grow with η, with the waves of contraction requiring a far higher power input than the waves of expansion.

When $D \to 0$, the tube becomes infinitely flexible and the resistance to the imposed force is provided purely by the fluid lubrication pressure. In this case, the forcing immediately sets the pressure, and (2.14) and (2.18) become analytically solvable algebraic problems for the tube radius. However, these problems admit discontinuous solutions at larger forcing amplitudes, a feature connected to the fact that the time-dependent version of our model (2.12) becomes hyperbolic in this limit (cf. Cowley 1982 and Balmforth *et al.* 2010; see also, for example, Lister 1992 and Ashmore, Hosoi & Stone 2003, for related thin-film problems). The discontinuous shocks become regularized by adding a small amount of stiffness, as outlined in Appendix A, which summarizes the main features of the $D \ll 1$ solutions.

Another analytically tractable limit is that of large bending stiffness, $D \gg 1$. In this situation, the tube wall can be significantly deformed only by introducing a correspondingly large forcing amplitude: $\eta \sim D \gg 1$. The main force balance in (2.11) then omits the fluid pressure, implying that the forcing should set the tube deformation independently of the flow dynamics, as in models prescribing the wall displacement (Fung & Yih 1968; Shapiro *et al.* 1969). As described in Appendix B, however, the lubrication pressure can only be safely ignored provided the tube does not become overly constricted, and a different solution strategy is required to deal with any occlusions.

3.3. *Flow patterns*

The steady flow patterns underneath the peristaltic waves are given by contours of the constant stream function,

$$\psi = -\frac{1}{16}r^2(2a^2 - r^2)\frac{\mathrm{d}p}{\mathrm{d}z} - \frac{1}{2}r^2, \tag{3.7}$$

obtained by integrating $w = r^{-1}\partial\psi/\partial r$. Examples for periodic waves with $n=0$ and forcing amplitudes of $\eta=2$ and $\eta=3$ are shown in figure 5. The geometry of the streamlines changes qualitatively between these two cases, with a recirculation

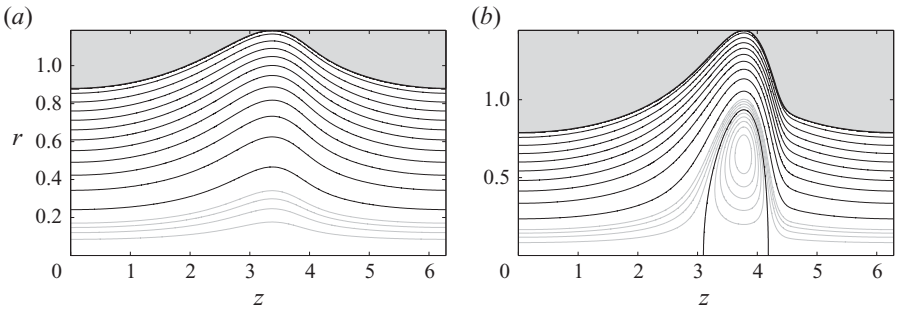

FIGURE 5. Streamlines for (*a*) $\eta = 2$ and (*b*) $\eta = 3$, with $D = 1$ and $n = 0$. Shown by the darker curves are 10 equally spaced contour levels; the lighter curves show additional contours near the tube centre. The lightly shaded region indicates the surrounding solid.

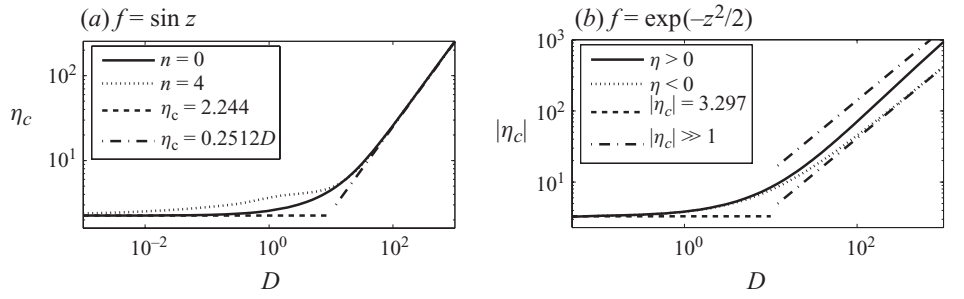

FIGURE 6. Critical wave amplitudes for the creation of recirculating fluid beneath (*a*) periodic waves and (*b*) solitary waves. In (*a*), critical amplitudes for both $n = 0$ and $n = 4$ are shown, along with the expected limits for $D \to 0$ and $D \gg 1$ derived in Appendices A and B. (*b*) Critical amplitudes for $n = 0$ with both $\eta > 0$ and $\eta < 0$, along with the $D \to 0$ and $D \gg 1$ limits (for the latter, $\eta_c \sim D\sqrt{2}$ or $\eta_c \sim -(\sqrt{2}-1)D$; see Appendix B).

cell appearing underneath the wave at an intermediate forcing strength (as found previously for fixed wall displacements, Shapiro *et al.* 1969). The critical forcing amplitude, $\eta = \eta_c$, at which a recirculation cell appears is determined by searching for flow speed reversals along the tube axis, which occur first when the maximum value of a^2 increases beyond $2(1-q)$ somewhere along the tube. Figure 6 illustrates how the critical amplitude (detected by monitoring $a^2 - 2(1-q)$ for the numerical solutions) varies with the stiffness of the wall (D), the type of forcing (periodic or solitary) and the choice of elastic solid ($n = 0$ or 4). At larger forcing amplitudes, the recirculation zones become extensive, with most of the fluid in the tube being conveyed along with the wave; figure 7 illustrates the flow patterns for some larger-amplitude waves.

4. Large-amplitude solutions

When $|\eta| \gg 1$, the properties of the large-amplitude peristaltic waves for all of the various cases can be constructed using asymptotic methods. Matched expansions are required for this task because different asymptotic solutions emerge over distinct sections of the tube, each reflecting different balances of the competing forces. Below, we give the leading-order form of these solutions, although we avoid a full description of the mathematical details in order to keep the discussion concise; Appendix C provides additional commentary on the matched asymptotics for $n = 0$ periodic waves.

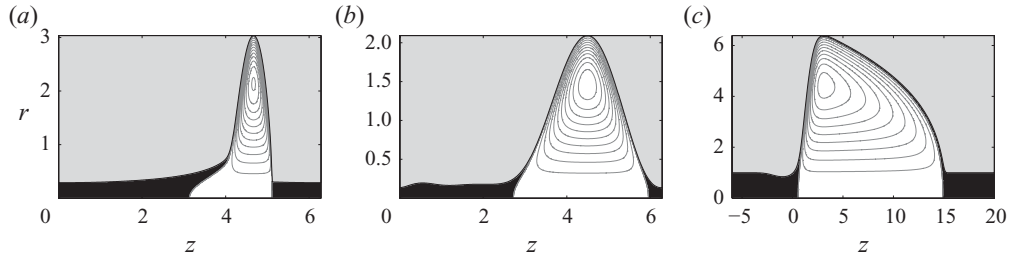

FIGURE 7. Streamlines for (*a*) a periodic wave with $n=0$ and $\eta=20$, (*b*) a periodic wave with $n=4$ and $\eta=30$ and (*c*) a solitary wave with $n=0$ and $\eta=12$ (all with $D=1$). Shown are 10 equally spaced contour levels highlighting the recirculation zone. The darker shaded region shows the fluid outside the recirculating core. The lightly shaded region indicates the surrounding solid.

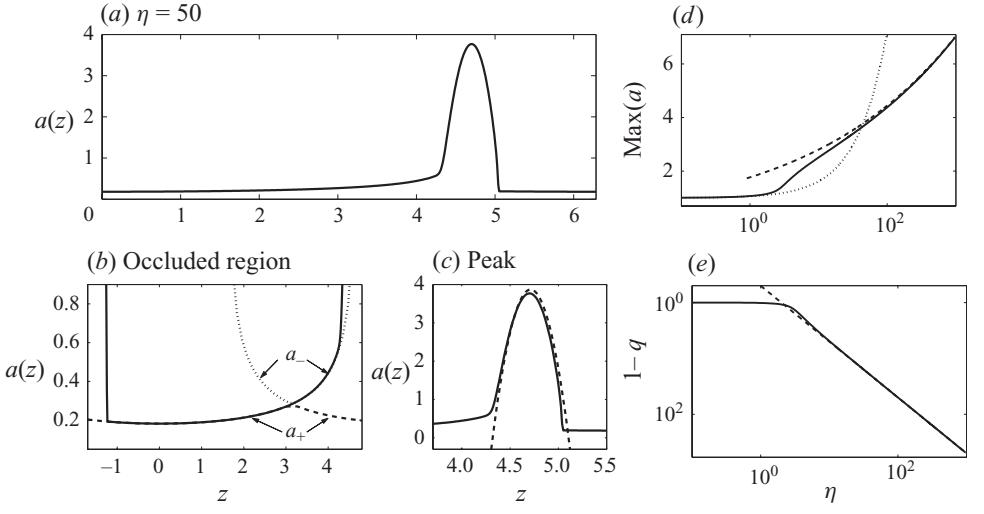

FIGURE 8. (*a*) A large-amplitude periodic wave for $n=0$, $D=1$ and $\eta=50$; magnifications of the occluded and blistered regions are shown in (*b*) and (*c*), where they are compared to the asymptotic solutions (4.2) for $a_{\pm}(z)$ (dashed and dotted lines in (*b*)), and the large-amplitude solution in (4.6) and (4.7) (dashed line in (*c*)). (*d*, *e*) The maximum wave amplitude and $1-q$ against η; the dotted and dashed lines show the low-amplitude and large-amplitude predictions, respectively (as given by $a \to 1+\eta a_1$ with (3.3) and $q \to 0$ for $\eta \ll 1$ and (4.3) and (4.11) for $\eta \gg 1$).

4.1. *Periodic waves for* $n=0$

For large-amplitude ($\eta \gg 1$) periodic waves, $q \to 1$ (corresponding to complete transport of fluid with the wave) and two qualitatively distinct regions develop in the wave profile. As illustrated by the sample solution in figure 8, a narrow, inflated blister appears near $z=3\pi/2$, with the remainder of the tube becoming substantially occluded. These features arise for both $n=0$ and $n=4$; we first deal with the former.

4.1.1. *The occlusion*

Because the tube radius is small in the occluded region, but the spatial scale is of order one, the dominant contribution to the pressure p in (2.11) arises from the forcing $\eta f(z)$. Equation (2.13) then reduces to the algebraic problem,

$$8(1-q)-8a^2-\eta a^4\cos z \approx 0, \tag{4.1}$$

which is independent of the stiffness of the tube, D (provided that parameter remains of order one), and reflects how the primary balance in the occlusion is between the forcing and the fluid lubrication pressure. Thus,

$$a \approx a_{\pm}(z) = \left[\frac{4}{\eta\cos z}\left(-1 \pm \sqrt{1+\frac{\eta}{2}(1-q)\cos z}\right)\right]^{1/2}. \tag{4.2}$$

As shown in figure 8, neither of the possibilities, $a_{\pm}(z)$, correspond fully to the occluded solution. Instead, $a(z)$ traces out the curve, $a_{+}(z)$, for $z < \pi$, but then switches to follow $a_{-}(z)$ in $z > \pi$. Crucially, in order that $a(z)$ remain continuous and smooth at $z = \pi$, a connection between the $a_{\pm}(z)$ curves is required there, which, given (4.2), can only be possible if

$$q \approx 1 - 2\eta^{-1}. \tag{4.3}$$

Substituting (4.3) into (4.2), and bearing in mind the specific progression of the solution along the two curves, then gives the solution for the tube radius in the occluded region $-\pi/2 < z < 3\pi/2$,

$$a \approx \frac{2}{\sqrt{\eta}}\left(1+\sqrt{2}\cos\frac{z}{2}\right)^{-1/2}. \tag{4.4}$$

4.1.2. *The blister*

For the blister, a becomes large over a relatively narrow region surrounding $3\pi/2$, allowing the stiffness term in (2.11) to compete with the forcing, and leading to

$$p_z \approx Da_z + \eta\left(z - \tfrac{3}{2}\pi\right). \tag{4.5}$$

Moreover, because the tube is occluded elsewhere, the blister must contain most of the fluid and therefore dominates the mass conservation constraint (2.15). Taken together, these details determine the characteristic width and amplitude of the blister, which we translate into the rescalings,

$$\zeta = \eta^{2/5}\left(z - \frac{3\pi}{2}\right), \qquad a = \eta^{1/5}A(\zeta). \tag{4.6}$$

Hence, to leading order, (2.13) can be reduced to $0 \approx (A^4/8)(D\,\mathrm{d}A/\mathrm{d}z + \zeta)$, which furnishes

$$A \approx A_{max} - \frac{\zeta^2}{2D}, \tag{4.7}$$

where A_{max} is the maximum rescaled tube radius. Returning to (2.11), we then discover the pressure is almost uniform in the blister:

$$p \approx -\eta - \eta^{1/5}DA_{max}. \tag{4.8}$$

In other words, there is a balance between tube stiffness, the forcing and a constant inflation pressure over the blister, with fluid flow playing no role.

As we describe in more detail in Appendix C, the blister solution must be matched to that for the occlusion through intervening boundary layers at $z \sim 3\pi/2 \pm \eta^{-2/5}\delta$ or $\zeta = \pm\delta$. In order to complete the determination of the leading-order blister solution, however, the detailed structure of the boundary layers is not needed, and one is required only to force $A(\zeta)$ to vanish at $\zeta = \pm\delta$ in order to ensure a successful match with the occlusion. Thus,

$$\delta = \sqrt{2DA_{max}}. \tag{4.9}$$

Finally, the leading-order version of the constraint (2.15) is

$$\int_{-\delta}^{\delta} A^2 \, \mathrm{d}\zeta \approx 2\pi, \tag{4.10}$$

which indicates that

$$\mathrm{Max}(a) = \eta^{1/5} A_{max} \approx \left(\frac{15^2 \pi^2 \eta}{2^3 D} \right)^{1/5}. \tag{4.11}$$

The solution in (4.7) and (4.11) is compared with the numerical results in figure 8.

Note that, although most of the fluid is carried along by the blister, the dissipation occurs primarily in the occlusion. By substituting (4.4) into (2.24), we obtain $\varepsilon \to 4\pi(2\pi - 4)$, implying that the increased dissipation occurring over the occlusion as the forcing strength is raised is countered by the additional constriction of that region. Simultaneously, the pumping efficacy, $2\pi^2 q/\varepsilon$, approaches $\pi/(4\pi - 8)$, which is enhanced by a factor of more than two over the value at low amplitude (1/4).

4.2. *Periodic waves with* $n = 4$

For $n = 4$, the construction of large-amplitude wave profiles proceeds along similar lines, although the characteristic scalings are different for the occlusion and blister, which reflects a slightly different character to the dynamics of the occlusions and boundary layers. In particular, although the small radius of the occlusion still ensures that the pressure is dictated largely by the forcing, $p \approx \eta \sin z$, it turns out that $1 - q \gg a^4 |\mathrm{d}p/\mathrm{d}z|/8$, and so (2.13) reduces to $a^2 \approx 1 - q$ over the occluded region. That is, the occlusion is too narrow to allow variations in fluid pressure to generate appreciable lubrication pressure or fluid flow. Thus, (2.13) reduces to an expression of constant mass transport due to the rigid translation of the cylindrical occlusion in the wave frame. However, although this exposes the main physical balances and the relation, $a \approx \sqrt{1 - q}$, it does not determine the characteristic scalings of either a or $1 - q$ with η.

For the blister, the combination of (2.14) and (2.15) implies the rescalings,

$$\zeta = \eta^{2/13} \left(z - \frac{3\pi}{2} \right), \qquad a = \eta^{1/13} A(\zeta). \tag{4.12}$$

We then solve the reduced version of (2.14), namely

$$D \frac{\mathrm{d}^5 A}{\mathrm{d}\zeta^5} \approx -\zeta, \tag{4.13}$$

subject to the requirement that the solution match the low-amplitude, flat occluded solution outside the blister. The match now amounts to demanding that $A = \mathrm{d}A/\mathrm{d}\zeta = \mathrm{d}^2 A/\mathrm{d}\zeta^2 = 0$ at the edges, $\zeta = \pm\delta$. In tandem with the leading-order version of the constraint (2.15), i.e. (4.10), we find

$$A \approx \frac{1}{6!\, D} (\delta^2 - \zeta^2)^3, \tag{4.14}$$

with

$$\delta = \pi^{1/13} (6!\, D)^{2/13} \left(\frac{11}{3} - \frac{20}{7} - \frac{6}{11} + \frac{1}{13} \right)^{-1/13}. \tag{4.15}$$

Note that the pressure within the blister is again predicted to be almost uniform: $p \sim -\eta + \eta^{9/13} \delta^2/10$. The asymptotic solution is compared with numerical results in figure 9, along with the prediction for the maximal radius, $\eta^{1/13} \delta^6/6!D$.

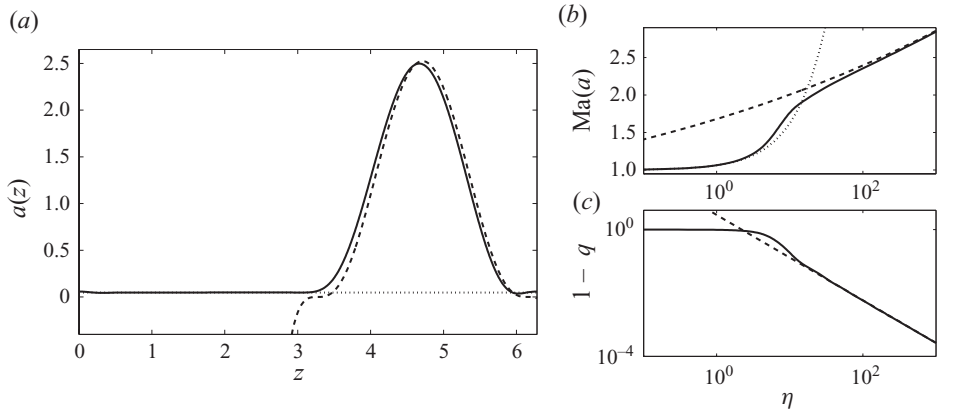

FIGURE 9. (*a*) A large-amplitude periodic wave for $n=4$, $D=1$ and $\eta=200$; the asymptotic solutions for the peak and occluded regions are indicated by the dashed and dotted lines ($a\sim\eta^{1/13}A$ with (4.14), and $a\sim\sqrt{1-q}$), respectively. (*b*, *c*) The maximum wave amplitude and $1-q$ against η; the dotted and dashed lines show the low-amplitude and large-amplitude limits ($\mathrm{Max}(a)\sim 1+\eta\ \mathrm{Max}(a_1)$, with (3.6), for $\eta\ll 1$, and $\mathrm{Max}(a)\sim\eta^{1/13}\delta^6/6!D$ and $1-q\sim 2.9\eta^{-35/26}$, with (4.15), for $\eta\gg 1$), respectively.

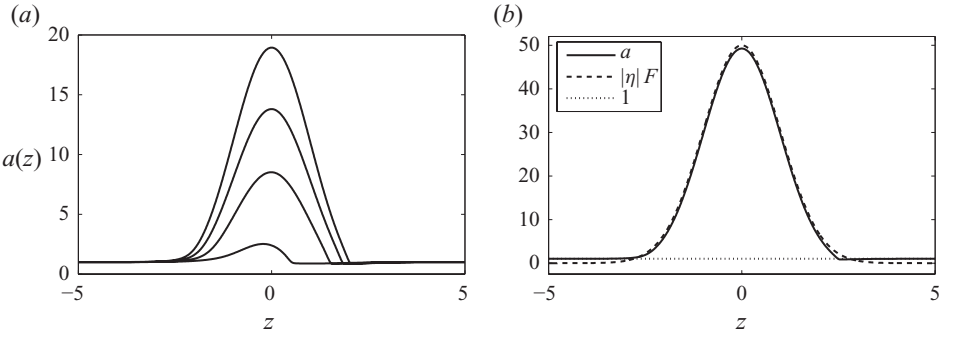

FIGURE 10. (*a*) Large-amplitude solitary-wave profiles for $n=0$, $D=1$ and $\eta=-5$, -10, -15 and -20. (*b*) Comparison of the $\eta=-50$ profile with the two pieces of the asymptotic solution, $a\sim 1$ and $a\sim|\eta|f(z)/D$.

Unlike the $n=0$ case, the transport correction, $1-q$, can only be found by a full matching of the solutions across the boundary layers intervening between the occluded and peak regions. Although we omit any detailed calculations here (which are rather more involved than those outlined in Appendix C), a scaling analysis of (2.14) and (4.14) shows that the boundary layers have thickness of order $\eta^{-21/52}$ and $1-q=O(\eta^{-35/26})$. This scaling agrees with the best fit to the numerical solutions, $(1-q)\sim 2.9\eta^{-35/26}$, shown in figure 9 for $D=1$. The physical interpretation of this result is that the boundary layers now act like bottlenecks in the flow, with the motion of the blister accomplished by a transference of fluid between those obstacles.

4.3. *Large-amplitude solitary waves for* $n=0$

Sample solitary-wave solutions with $|\eta|\gg 1$ are shown in figures 10 and 11. For $\eta<0$, illustrated in figure 10, another localized blister builds up as $|\eta|$ increases. Unlike the periodic waves, however, which must conserve mass according to the constraint (2.15), the remainder of the tube does not become occluded. Instead, the

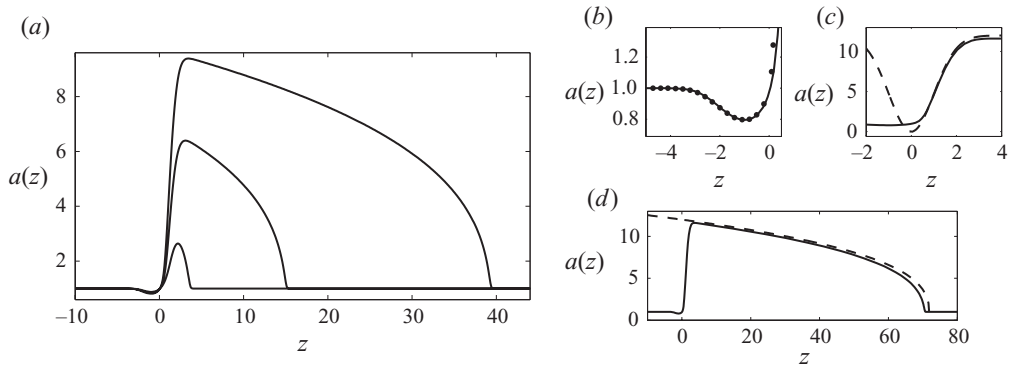

FIGURE 11. Large-amplitude solitary-wave profiles for $n=0$, $D=1$ and (a) $\eta=5$, 7.5 and 10, and (b)–(d) $\eta=12$. (b)–(d) Comparison of the wave profile with the three sections of the asymptotic solution: in (b), $a\sim[4/(\eta f')(\sqrt{1+\eta f'/2}-1)]^{1/2}$, in (c), $a\sim\eta(1-f)$ and in (d), $a\sim(\eta^3-24z/D)^{1/3}$.

large-amplitude blister must be matched to an undeformed tube, $a\approx 1$, through the narrow intervening boundary layers. The dominant balance over the blister (arising from equating the forcing with the tube stiffness) is $D\,\mathrm{d}a/\mathrm{d}z\sim\eta f'$ in (2.18), giving the profile, $a\sim|\eta|f(z)/D+constant$. The integration constant, and the position and thickness of the boundary layers, must be found by matching. Detailed calculations show that the integration constant is of order one, so that two boundary layers must occur where $\eta f'(z)$ also becomes order one, or equivalently near $z=\pm\sqrt{2\log|\eta|}$. The downstream boundary layer is found to have a thickness of $O(1/\sqrt{2\log|\eta|})$, and further matching calculations over that region eventually furnish

$$a\sim\frac{|\eta|f(z)}{D}+1+O\big((2\log|\eta|)^{-1/2}\big). \tag{4.16}$$

The transport is dominated by the blister, and to leading order we find $\Delta\sim\eta^2\sqrt{\pi}/D^2$ (as shown earlier in figure 3).

The picture is rather different for waves of contraction (figure 11). For $\eta\gg 1$, the squeezing action of the forcing is partly countered by lubrication pressure, upsetting the balance $D\,\mathrm{d}a/\mathrm{d}z\sim\eta f'$ in (2.18). In fact, three characteristic regions emerge in the solution, as illustrated in figure 11$(a$–$d)$, each of which corresponds to a different balance of terms in (2.18). Ahead of the forcing, a long bow wave builds up that is controlled by fluid lubrication pressures and tube stiffness and is given by

$$D\frac{\mathrm{d}a}{\mathrm{d}z}\sim-\frac{8}{a^4}(a^2-1) \tag{4.17}$$

(as $f(z)$ is exponentially small there). To leading order, since a is large, $a\sim(a_{max}^3-24z/D)^{1/3}$ (see figure 11d), which is similar to Griffiths' (1987, 1989) model of a bolus in the ureter.

An occluded region near the point of maximal contraction is maintained by a combination of lubrication pressure and the forcing,

$$\eta f'(z)\sim-\frac{8}{a^4}(a^2-1), \tag{4.18}$$

which can again be solved algebraically, this time with a unique, unambiguous choice for the solution (the analogue of a_+ in (4.2); see figure 11b). The solution of (4.18) is

of order $\eta^{-1/4}$, where $f'(z)$ is of order one, but $a \to 1$ further to the left, where $f'(z)$ becomes exponentially small. Although the stiffness term can no longer be neglected in (4.18) for this latter stage, there is no significant change to $a \approx 1$.

The profile increases from the $O(\eta^{-1/4})$ trailing wave to the $O(a_{max})$ bow wave over a central core in which the main balance omits the lubrication pressure, $D\,\mathrm{d}a/\mathrm{d}z \sim -\eta f'(z)$. Since a must match to the low-amplitude trailing solution in (4.18), we find $a \sim \eta[1-f(z)]/D$ (see figure 11*c*). The match to the precursor bow wave then implies $a_{max} = \eta/D$. Thus, the bow wave extends a distance $\eta^3/24D^2$ ahead of the forcing. Finally, the transport, which is dominated by the bow wave, can be estimated to be $\Delta \sim \eta^5/40D^5$ (see figure 3).

For the large-amplitude solitary waves, the dissipation takes place mostly in the inflated regions of the tube (the bow wave for $\eta > 0$ or the large-amplitude blister for $\eta < 0$), implying ε in (2.24) is simply given by 8π multiplied by the length of those inflations. For the wave of contraction, the bow wave provides $\varepsilon \sim \eta^3/3D^2$. For the expansion wave, on the other hand, the dissipation rate takes a logarithmic dependence on forcing amplitude: $\varepsilon \sim 16\sqrt{2\log(-\eta/D)}$. Although large-amplitude solitary waves require a large input of power, they perform better than periodic waves due to the larger quantities of transported fluid: the solitary-wave pumping efficacy is either $\Delta/\varepsilon \sim \eta^2\sqrt{\pi/2}/(16D^2\sqrt{\log|\eta|/D})$ for $\eta < 0$, or $\Delta/\varepsilon \sim 3\eta^2/40D^3$ for $\eta > 0$.

5. Discussion

In this article, we have presented a lubrication theory for nonlinear peristaltic waves driven by a force acting on the elastic tube wall. We have built small- and large-amplitude solutions asymptotically, and spanned the gap between those limits with numerical solutions. In the appendices, we give further discussion of the limits of small and large tube stiffness, which offer further analytical inroads to the problem. We close by generalizing some of the results, focusing on the high-amplitude limit, as low-amplitude waves have received more attention in existing literature.

For periodic waves, the conservation of fluid volume imposes a significant constraint on the nonlinear solutions: as the forcing amplitude increases, narrow inflated blisters form on the tube, drawing in and transporting most of the fluid; the remainder of the duct becomes severely occluded in order to accommodate the rearrangement of fluid. The blister arises where the outward force is maximized; provided the force is locally parabolic in the axial coordinate (z), our asymptotic scalings imply

$$a_{max} \sim \eta^{1/(2n+5)}, \qquad \text{and} \qquad \delta \sim \eta^{-2/(2n+5)}, \tag{5.1}$$

for the maximum radius of the blister and its characteristic length, given the forcing amplitude, η, and the largest axial derivative, n, in the force law for the elastic wall. This result relies on the linearity of the elastic model for the tube, and emerges from the combination of global mass conservation and the force balance, which is dominated by the imposed forcing, the elastic resistance and a constant pressure in the fluid bubble underneath the blister. To arrive at the scalings in (5.1), we first note that (2.11) implies $p \sim \eta f(z_{max})$ and $\mathrm{d}p/\mathrm{d}z \sim D\mathrm{d}^{n+1}a/\mathrm{d}z^{n+1} + \eta f''(z_{max})(z - z_{max}) \sim 0$, where z_{max} is the position of the maximum inward force. One then estimates that $A_{max} \sim \eta\delta^{2+n}$. Finally, the mass conservation constraint implies the further scaling $\delta A_{max}^2 \sim O(1)$, leading to (5.1).

For solitary waves, we focused on just one elastic model ($n = 0$). Waves of compression are very different from those of expansion (except at low amplitude)

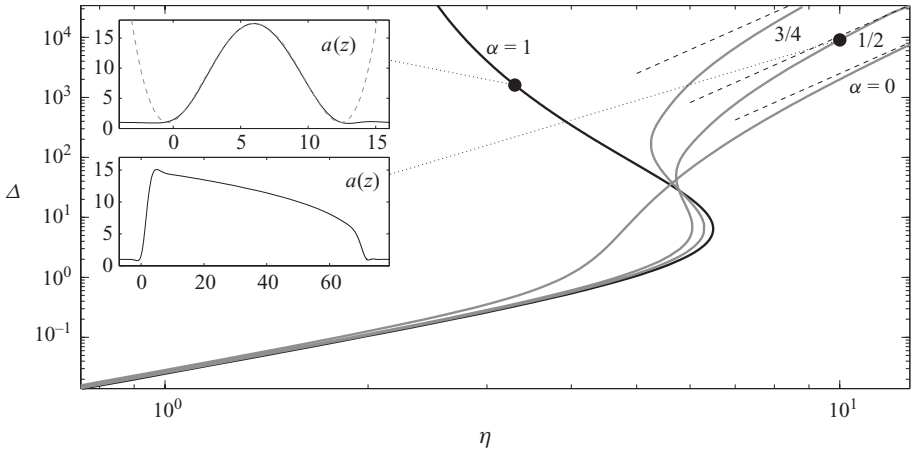

FIGURE 12. The main figure shows the transport Δ against η of numerical solutions for solitary waves with the resistance law (2.5), $n=4$ and $D=1$. Shown are data for $\alpha=1/2$ and 3/4, together with $\alpha=1$ (our earlier '$n=4$ case') and $\alpha=0$ (the '$n=0$ case' above). The large-η limit, $\Delta\sim[\eta/(1-\alpha)D]^5$, is shown by dashed lines. The insets show two sample large-amplitude solutions. The example for $\alpha=1$ also includes an approximating quartic polynomial (dashed curve).

although both are able to transport fluid. The solitary wave of expansion creates a translating, inflated blister with radius $a\sim\eta/D$, which transports most of the fluid (giving $\Delta=\int(a^2-1)\,\mathrm{d}z\sim\eta^2/D^2$). The compressive solitary wave, on the other hand, cannot squeeze the tube to small radii without building up lubrication pressures; the elevated pressures underneath the forcing then drive a long bow wave which transports a much larger amount of fluid ($\Delta\sim\eta^5/D^5$) even though the maximum radius remains of the order of η/D. The bow wave represents a balance between the trail off in fluid pressure and the elastic forces, and therefore depends on the detailed solid mechanics.

Our focus on solitary waves with $n=0$ was in part because the $n=4$ solutions could not be extended to high amplitude; as illustrated in figure 12, the solution branch corresponding to these waves reaches a finite maximum value of η and then turns around to proceed back to smaller forcing amplitude, with the tube deformations increasing all the while. The solution appears to diverge as η approaches a value near two, developing a long bow wave with a relatively simple spatial structure (see figure 12). A similar singular behaviour also occurs for waves of expansion.

The turnaround in figure 12 and the absence of peristaltic waves at higher forcing amplitude is critically dependent on the $n=4$ elastic force law. More specifically, returning to the more general resistance model in (2.5), we observe that a re-introduction of the first term with $\alpha\neq1$ changes the picture entirely: for $\alpha<1$, the first turn-around is followed by a second one, with the branch then resuming its progression to large forcing amplitude. This leads to solutions that follow the low-amplitude $(n,\alpha)=(4,1)$ solution branch at smaller η, but then converge for $\eta\gg1$ to a high-amplitude $(n,\alpha)=(0,0)$ branch with a modified stiffness parameter of $(1-\alpha)D$. Similar bifurcation curves were found by Kriegsmann, Miksis & Vanden-Broeck (1998) in a somewhat similar thin-film problem.

Note that the spatial structure of the forcing has played little role in establishing many of the salient details of our solutions, and so we do not regard our choices of sinusoidal or Gaussian forcings as significant. By contrast, the dynamics is sensitive

to the solid mechanics and it is difficult to say how many of the results apply to general tube models, especially when nonlinear deformations are taken into account in the large-amplitude limit. Other limitations of our model include the restriction to Stokes flow and long peristaltic waves (i.e. the lubrication approximation, which may fail for the relatively steep, large-amplitude solutions that we have presented), and the fact that the stresses on the wall might cause the structure to rupture or buckle, further limiting the driving stresses.

Finally, in many biological ducts, peristalsis is required to transport more varied contents than a viscous fluid. In some situations, the fluid suspends solid particles or is non-Newtonian. In the companion paper (Takagi & Balmforth 2011) we continue our exploration by exploring the peristaltic transport of a fluid containing a rigid object. Although the pumping of viscoelastic liquids has already received some attention (e.g. Bohme & Friedrich 1983), fluids that act like solids until a critical stress is reached (i.e. viscoplastic fluids) have received far less attention (although Vajravelu, Sreenadh & Ramesh Babu 2005 have generalized the fixed-displacement, peristaltic lubrication models to Herschel–Bulkley fluids). One of our goals in future work is to generalize the current model to accommodate fluid viscoplasticity; our initial work in this direction is summarized by Takagi (2009).

This research began at the 2009 Geophysical Fluid Dynamics Summer Program, Woods Hole Oceanographic Institution, which is supported by the National Science Foundation and the Office of Naval Research. We thank the participants for discussions, especially W. R. Young and J. B. Keller.

Appendix A. The limit of vanishing stiffness

With $D=0$, the parameter n is irrelevant and (2.13) reduces to

$$q = 1 - a^2 - \frac{1}{8}\eta a^4 f'(z), \tag{A 1}$$

with solution,

$$a^2 = a_\pm^2(z) = \frac{4}{\eta f'(z)}\left[-1 \pm \sqrt{1 + \frac{1}{2}(1-q)\eta f'}\right]. \tag{A 2}$$

Provided $\eta < \eta_s = 2/[(1-q)\ \mathrm{Min}(f')]$, the selection $a = a_+(z)$ provides the correct solution; the alternative, $a = a_-(z)$, is unphysical and provides a real solution only where $f' < 0$. This is illustrated in figure 13, which shows periodic numerical solutions for small but finite D ($D=0.02$) and $n=0$, and which match up with $a = a_+(z)$ provided $\eta < \eta_s \approx 2.244$.

At $\eta = \eta_s$, the solutions develop a corner corresponding to a connection arising between a_+ and a_- at $z=\pi$, and for higher forcing amplitudes the solutions become discontinuous. The slightly stiff numerical solutions for $\eta > \eta_s$ continue to trace out the $a = a_+(z)$ curve for part of the domain. However, they also pass onto the $a_-(z)$ curve on proceeding through $z=\pi$, remaining close to that curve until abruptly jumping back down to the $a_+(z)$ curve in a regularized shock. The passage of the regularized solution through the intersection of the $a_+(z)$ and $a_-(z)$ curves at $z=\pi$ demands that

$$q = 1 - \frac{2}{\eta} \tag{A 3}$$

(cf. the inset to figure 13*a*).

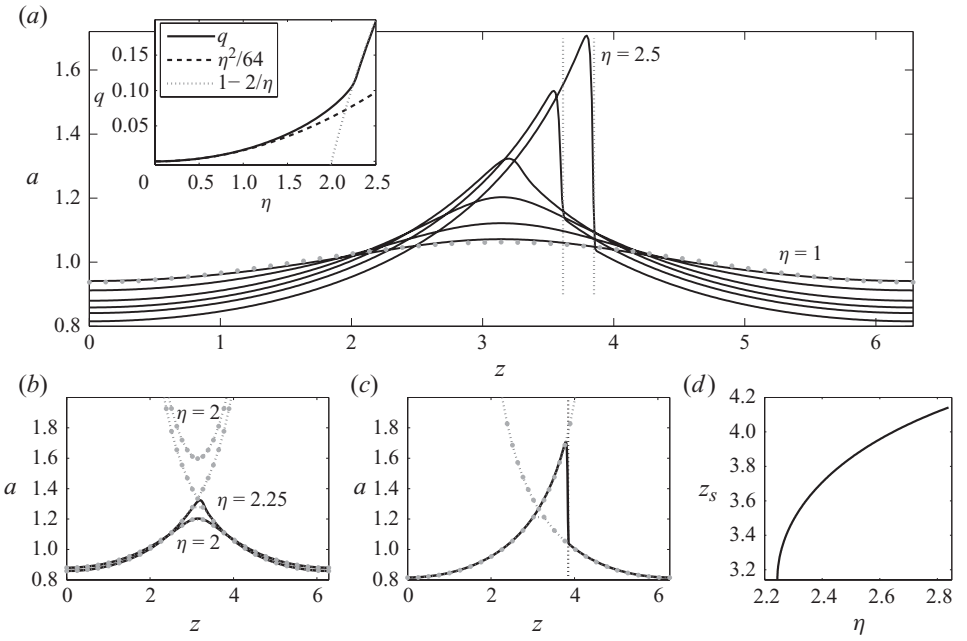

FIGURE 13. Periodic wave profiles for $D=0.02$ and $n=0$. (*a*) Profiles with $\eta=1$, 1.5, 2, 2.25, 2.35 and 2.5; the dots show the low-amplitude prediction (3.3) with $\eta=1$, and the vertical dotted lines indicate the expected shock positions for $\eta=2.35$ and 2.5. The inset shows the flux q, along with the limits (3.4) and (A 3). (*b*, *c*) Comparison of the wave profiles (for $\eta=2$ and 2.25, and $\eta=2.5$, respectively) with the $D=0$ solutions in (A 2). (*d*) The shock position against η.

The shock position, $z=z_s$, for $D\to 0$ can be determined by applying the constraint, $\langle a^2\rangle=1$, to the limiting solution,

$$a \sim \frac{2}{\sqrt{\eta}}\left(1+\sqrt{2}\cos\frac{z}{2}\right)^{-1/2}, \tag{A 4}$$

in the domain $z_s-2\pi<z<z_s$. Thence, we arrive at the implicit equation,

$$\frac{1}{2}\pi\eta=\int_{z_s-2\pi}^{z_s}\left(1+\sqrt{2}\cos\frac{z}{2}\right)^{-1}\mathrm{d}z \tag{A 5}$$

(the integrals can be performed analytically though the result is not particularly transparent). Setting $z_s\to\pi$ and evaluating the integral leads to the critical value,

$$\eta_s=\frac{8}{\pi}\ln(\sqrt{2}+1)\approx 2.244. \tag{A 6}$$

For solitary waves, the construction of the solutions is rather different. Because $q=0$, we discover immediately that $|\eta_s|=2\mathrm{e}^{1/2}\approx 3.297$ for our Gaussian forcing. Moreover, for $|\eta|>|\eta_s|$, neither of the $D=0$ solutions remain physical as they both become complex over a range of z surrounding $z=1$. The slightly stiff numerical solutions find their way past this conundrum by quickly adopting a form like the large-amplitude solitary-wave solutions of the main text (see figure 14). In other words, there is no $D=0$ limit for solitary waves; the wave amplitudes increase without limit for $D\to 0$.

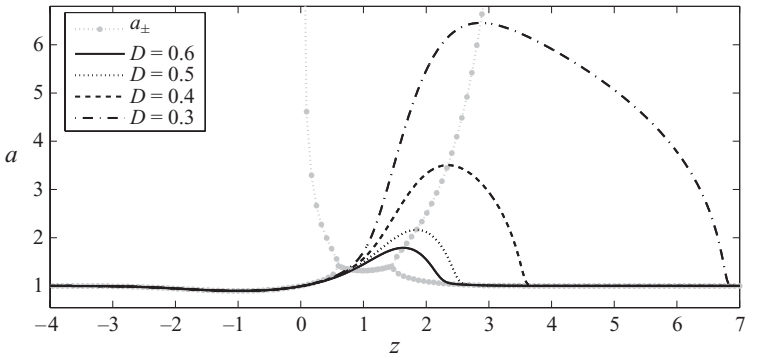

FIGURE 14. Solitary-wave profiles for $\eta = 4$, $n = 0$ and varying D (0.6, 0.5, 0.4 and 0.3). The dots show $a_\pm(z)$ from (A 2), which merge and become complex over a range surrounding $z = 1$.

Note that the criterion for recirculation in the limit $D \to 0$ becomes equivalent to that for the formation of the shock: $w(0, z) = -1 - a^2 p_z/4 \to -1 - \eta a^2 f'/4$, which cannot vanish if $a = a_+(z)$ and that curve does not meet $a_-(z)$ at the minimum of $f'(z)$.

Appendix B. Large stiffness

For $D \gg 1$ and $|\eta|/D = O(1)$,

$$D \frac{\mathrm{d}^{1+n} a}{\mathrm{d}z^{1+n}} \sim \eta f'(z), \tag{B 1}$$

and we find the periodic wave solution,

$$a \sim \sqrt{1 - \frac{\eta^2}{2D^2}} - \frac{\eta}{D} \sin z \tag{B 2}$$

and

$$q = 1 - \frac{\langle a^{-2} \rangle}{\langle a^{-4} \rangle} \sim \frac{\eta^2 (16D^2 - 9\eta^2)}{4D^2(\eta^2 + D^2)}. \tag{B 3}$$

This solution only makes sense provided $\eta < D\sqrt{2/3}$, as otherwise the solution for the radius does not remain positive over the whole domain. Instead, the tube is prevented from becoming too constricted by the lubrication pressure; for $\eta > D\sqrt{2/3}$, the wave profiles develop flat minima with $a \ll 1$ but bear many similarities to the large-amplitude solutions in the main text. The criterion for the appearance of recirculation beneath the wave (arising for $\eta < D\sqrt{2/3}$) is $w(0, z) < 0$, or $2(1 - q) < a^2$, which occurs first for $z = \pi/2$ and $2(1 - q) = [(\eta/D) + \sqrt{1 - (\eta^2/2D^2)}]$. Thus, $\eta_c \approx 0.2512D$ (cf. figure 6).

In the infinite domain, and considering the case $n = 0$, the large-stiffness solution is $a \sim 1 - \eta f(z)/D$, provided $\eta < D$. Waves of expansion ($\eta < 0$) converge without difficulty to this solution (figure 15), and the criterion for recirculation, $a^2 > 2$, reduces to $|\eta| \geqslant \eta_c = (\sqrt{2} - 1)D$. On the other hand, for waves of contraction, the solution $a \sim 1 - \eta f(z)/D$ predicts negative radii if $\eta > D$. Such regions are prevented by increased lubrication pressures, and a constriction develops within the forced region; see figure 15. A pressure jump forms across the constriction such that $a \sim 1 - \eta f/D$ to the left, and $a \sim 1 + (P - \eta f)/D$ to the right, where P denotes the pressure jump. The

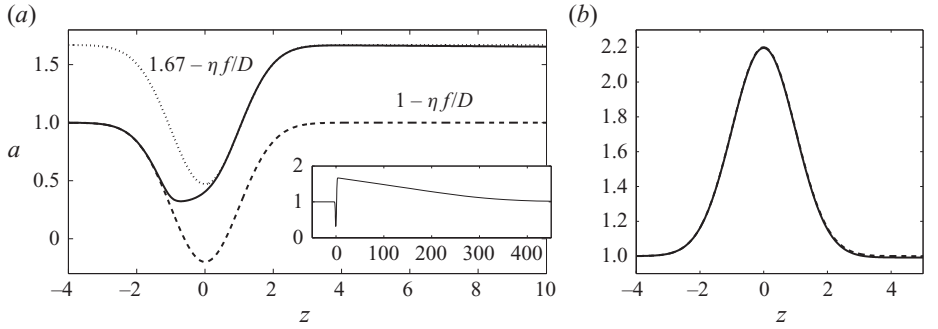

FIGURE 15. Solitary-wave profiles for $n=0$, $D=10^3$ and (*a*) $\eta=1200$ and (*b*) $\eta=-1200$. The dashed curve shows $1-\eta f(z)/D$, and the dotted curve in (*a*) shows $1.67-\eta f(z)/D$. The inset of (*a*) shows the full, spatially extended wave profile.

elevated pressures upstream of the constriction are relieved within a long bow wave, as in the large-amplitude solutions considered in the main text. The constriction itself is controlled by a balance between lubrication pressures and the forcing, leading to $a\sim(8/\eta f')^{1/4}$. The balance can only be maintained for $f'>0$, or $z<0$, and coupled with the need to match to the solutions outside the constriction, it follows that the constriction occupies the region, $-\sqrt{2\log(\eta/D)}<z<0$, and $P\equiv\eta-D$ (the solution in figure 15 has not yet converged to the limiting pressure jump). The tube therefore bulges out to a radius η/D, and the bow wave is given implicitly by

$$\frac{8z}{D}=\frac{1}{2}\log\frac{(a+1)(\eta-D)}{(a-1)(\eta+D)}-a-\frac{a^3}{3}+\frac{\eta}{D}+\frac{\eta^3}{3D^3}. \tag{B 4}$$

The recirculation condition is $\eta>\eta_c=D\sqrt{2}$.

Appendix C. Matched asymptotics and boundary layers for periodic, $n=0$ waves

For our $n=0$ periodic waves, the governing equation can be reduced to

$$\frac{1}{8}a^4\left(D\frac{\mathrm{d}a}{\mathrm{d}z}+\eta\cos z\right)+a^2=1-q. \tag{C 1}$$

For the occlusion, the amplitude is small, z is order one and $1\gg(1-q)$. The bending term, $D\,\mathrm{d}a/\mathrm{d}z$, is therefore small in comparison to the forcing, $\eta\cos z$, and demanding that a^2 and $1-q$ are of the same order as the forcing guides us to the asymptotic sequences,

$$a=\eta^{-1/2}a_{1/2}+\ldots,\quad q=1-\eta^{-1}q_1+\ldots, \tag{C 2}$$

which are implicit in (4.1).

The blister is narrow, $|z-3\pi/2|\ll1$, and has a large amplitude, $a\gg1$, indicating that it dominates the constraint, $\langle a^2\rangle=1$ (which relates the width and amplitude scalings). The left-hand side of (C 1) now dominates the right, and after estimating the size of its three constituent terms (and thereby neglecting the final one), we arrive at the scalings in (4.6) and

$$D\frac{\mathrm{d}A}{\mathrm{d}\zeta}+\zeta=O(\eta^{-1}), \tag{C 3}$$

with solution (4.7). Reconstruction of the leading-order pressure then furnishes (4.8).

The transition layers between the occluded portions of the tube and the blister are centred at $z = 3\pi/2 \pm \eta^{-2/5}\delta$. Here, $\eta f' \sim \pm \eta^{3/5}\delta$, and to leading order (C 1) reduces to

$$D\frac{\mathrm{d}a}{\mathrm{d}z} \sim \frac{1}{a^4}\left(\frac{16}{\eta} - 8a^2 \mp \eta^{3/5}\delta a^4\right). \tag{C 4}$$

This first-order equation has a fixed point given by the right-hand side which is connected by (C 4) to a diverging, $a \gg 1$, solution dictated by $D\,\mathrm{d}a/\mathrm{d}z \to \mp\eta^{3/5}\delta$. The fixed point corresponds to the limit of the occluded solution in the transition layers, whereas the large-amplitude solution corresponds to the limit of the blister solution.

For $z \sim 3\pi/2 - \eta^{-2/5}\delta$ (the left edge of the blister), the fixed point is given by neglecting the first term on the right of (C 4), which furnishes the correct match with the limit of the occluded solution in (4.4), namely $a \sim 2\eta^{-3/10}\sqrt{2/\delta}$. Balancing all the remaining terms in (C 4) then implies that the transition layer at the left edge of the blister has a characteristic thickness of order $\eta^{-9/10}$. For $z \sim 3\pi/2 + \eta^{-2/5}\delta$, on the other hand, the fixed point that matches the limit of (4.4) is given by $a \sim \sqrt{2/\eta}$, which requires us to neglect the final term on the right of (C 4). Balancing all the remaining terms then indicates that the transition layer at the right edge of the blister has a thickness of order $\eta^{-3/2}$.

Equation (C 4) can be tackled with asymptotic methods to complete a formal matched expansion. Alternatively, (C 4) can be integrated directly to furnish an implicit solution for a, or solved graphically for the qualitative form of the solution. For the present purposes, we emphasize only that this solution smoothly connects the occluded and peak solutions. The main ramification of this connection is to demand that the leading-order peak solution, $\eta^{1/5}A(\zeta)$, vanish at the edges of the blister, leading to (4.9). (In other words, the matching across the boundary layers can be effected by 'patching' the blister to the occlusion at the blister's edges.)

REFERENCES

Argentina, M., Skotheim, J. & Mahadevan, L. 2007 Settling and swimming of flexible fluid-lubricated foils. *Phys. Rev. Lett.* **99** (22), 224503.

Ashmore, J., Hosoi, A. E. & Stone, H. A. 2003 The effect of surface tension on rimming flows in a partially filled rotating cylinder. *J. Fluid Mech.* **479**, 65–98.

Balmforth, N. J., Coombs, D. & Pachman, S. 2010 Microelastohydrodynamics of swimming organisms near solid boundaries in complex fluids. *Q. J. Mech. Appl. Maths* **63**, 267–294.

Bohme, G. & Friedrich, R. 1983 Peristaltic flow of viscoelastic liquids. *J. Fluid Mech.* **128**, 109–122.

Brasseur, J. 1987 A fluid mechanical perspective on esophageal bolus transport. *Dysphagia* **2** (1), 32–39.

Carew, E. O. & Pedley, T. J. 1997 An active membrane model for peristaltic pumping. Part I. Periodic activation waves in an infinite tube. *J. Biomech. Engng* **119**, 66–76.

Chan, D., Balmforth, N. J. & Hosoi, A. 2005 Building a better snail: lubrication theory and adhesive locomotion. *Phys. Fluids*, **17**, 113101.

Cowley, S. J. 1982 Elastic jumps on fluid-filled elastic tubes. *J. Fluid Mech.* **116**, 459–473.

Fung, Y. C. 1971 Peristaltic pumping: a bioengineering model. In *Urodynamics: Hydrodynamics of the Ureter and Renal Pelvis* (ed. S. Boyarsky *et al.*), pp. 178–198. Academic.

Fung, Y. C. & Yih, C. S. 1968 Peristaltic transport. *J. Appl. Mech.* **35**, 669–675.

Griffiths, D. J. 1987 Dynamics of the upper urinary tract. Part I. Peristaltic flow through a distensible tube of limited length. *Phys. Med. Biol.* **32**, 813–822.

Griffiths, D. J. 1989 Flow of urine through the ureter: a collapsible, muscular tube undergoing peristalsis. *J. Biomech. Engng* **111**, 206–211.

Katz, D. F. 1974 On the propulsion of micro-organisms near solid boundaries. *J. Fluid Mech.* **64**, 33–49.

Keller, J. & Falkovitz, M. 1983 Crawling of worms. *J. Theor. Biol.* **104** (3), 417–442.

Kerr, A. D. 1984 On the formal development of elastic foundation models. *Ing.-Archiv.* **64**, 455–464.

Kriegsmann, J. J., Miksis, M. J. & Vanden-Broeck, J. M. 1998 Pressure driven disturbances on a thin viscous film. *Phys. Fluids* **10**, 1249.

Li, M. & Brasseur, J. G. 1993 Non-steady peristaltic transport in finite-length tubes. *J. Fluid Mech.* **248**, 129–151.

Lister, J. R. 1992 Viscous flows down an inclined plane from point and line sources. *J. Fluid Mech.* **242**, 631–653.

Lykoudis, P. & Roos, R. 1970 The fluid mechanics of the ureter from a lubrication theory point of view. *J. Fluid Mech.* **43** (4), 661–674.

Miftakhov, R. & Wingate, D. 1994 Numerical simulation of the peristaltic reflex of the small bowel. *Biorheology* **31** (4), 309–325.

Pozrikidis, C. 1987 A study of peristaltic flow. *J. Fluid Mech.* **180**, 515–527.

Shapiro, A. H., Jaffrin, M. Y. & Weinberg, S. L. 1969 Peristaltic pumping with long wavelengths at low Reynolds number. *J. Fluid Mech.* **37**, 799–825.

Skotheim, J. & Mahadevan, L. 2005 Soft lubrication: the elastohydrodynamics of conforming and non-conforming contacts. *Phys. Fluids* **17**, 092101.

Szeri, A. J., Park, S. C., Verguet, S., Weiss, A. & Katz, D. F. 2008 A model of transluminal flow of an anti-HIV microbicide vehicle: combined elastic squeezing and gravitational sliding. *Phys. Fluids* **20**, 083101.

Takabatake, S., Ayukawa, K. & Mori, A. 1969 Peristaltic pumping in circular cylindrical tubes: a numerical study of fluid transport and its efficiency. *J. Fluid Mech.* **193**, 267–283.

Takagi, D. 2009 Nonlinear peristaltic waves: a bitter pill to swallow. In *Proceedings of the 2009 Summer Study Program in Geophysical Fluid Dynamics*, Woods Hole Oceanographic Institution, USA.

Takagi, D. & Balmforth, N. J. 2011 Peristaltic pumping of rigid objects in an elastic tube. *J. Fluid Mech.* **672**, 219–244.

Tang, D. & Rankin, S. 1993 Numerical and asymptotic solutions for peristaltic motion of nonlinear viscous flows with elastic free boundaries. *SIAM J. Sci. Comput.* **14**, 1300–1319.

Taylor, G. 1951 Analysis of the swimming of microscopic organisms. *Proc. R. Soc. Lond.* A **209**, 447–461.

Timoshenko, S. P. & Woinowsky-Krieger, S. 1959 *Theory of Plates and Shells*. McGraw-Hill.

Vajravelu, K., Sreenadh, S. & Ramesh Babu, V. 2005 Peristaltic transport of a Herschel–Bulkley fluid in an inclined tube. *Intl J. Nonlinear Mech.* **40** (1), 83–90.

Walker, S. W. & Shelley, M. J. 2010 Shape optimization of peristaltic pumping. *J. Comput. Phys.* **229**, 1260–1291.

Yin, F. C. & Fung, Y. C. 1971 Mechanical properties of isolated mammalian ureteral segments. *Am. J. Physiol.* **221**, 1484–1493.